Article

Correlation between Magnetocaloric Properties and Magnetic Exchange Interaction in $Gd_{54}Fe_{36}B_{10-x}Si_x$ Amorphous Alloys

Huiyan Zhang [1,2,3,*], Jia Tan [3], Xue Zhang [3], Jiazhe Yan [3], Han Shi [2], Ye Zhu [3], Weizhong Cheng [3], Hailing Li [1,3], Weihuo Li [1,3,4] and Ailin Xia [1,3]

1   Key Laboratory of Green Fabrication and Surface Technology of Advanced Metal Materials, Anhui University of Technology, Ministry of Education, Ma'anshan 243002, China
2   Ma'anshan Shuntai Rare Earth New Materials Co., Ltd., Ma'anshan 243100, China
3   School of Material Science and Engineering, Anhui University of Technology, Ma'anshan 243002, China
4   Wuhu Technology and Innovation Research Institute, Anhui University of Technology, Wuhu 241003, China
*   Correspondence: hyzh2017@ahut.edu.cn

Abstract: $Gd_{54}Fe_{36}B_{10-x}Si_x$ ($x = 0, 2, 5, 8, 10$) amorphous ribbons were fabricated by melt-spinning technique. Based on the molecular field theory, the magnetic exchange interaction was analyzed by constructing the two-sublattice model and deriving the exchange constants J_{GdGd}, J_{GdFe} and J_{FeFe}. It was revealed that appropriate substitution content of Si for B can improve the thermal stability, maximum magnetic entropy change and widened table-like magnetocaloric effect of the alloys, while excessive Si will lead to the split of the crystallization exothermal peak, inflection-like magnetic transition and deterioration of magnetocaloric properties. These phenomena are probably correlated to the stronger atomic interaction of Fe-Si than that of Fe-B, which induced the compositional fluctuation or localized heterogeneity and then caused the different way of electron transfer and nonlinear variation in magnetic exchange constants, magnetic transition behavior and magnetocaloric performance. This work analyzes the effect of exchange interaction on magnetocaloric properties of Gd-TM amorphous alloys in detail.

Keywords: Gd-Fe-based amorphous alloys; magnetocaloric effect; magnetic transition behavior; molecular field theory; exchange interaction

1. Introduction

Magnetic refrigeration (MR) using solid magnetic material as a refrigerant has the advantages of environmental friendliness, low energy consumption and high efficiency. MR has been regarded as a potential alternative to replace traditional gas compression refrigeration [1]. The basic principle of MR is the intrinsic magnetocaloric effect (MCE) of magnetic materials: when a magnetic material is adiabatically magnetized, its total entropy S ($S = S_M + S_E + S_L$, where S_M, S_E and S_L denote magnetic entropy, electron entropy and lattice entropy, respectively) retains unchanged; the spin will align parallel to the direction of the applied magnetic field, inducing a decrease in S_M as well as an increase in S_E and S_L, and therefore the enhanced lattice vibration leads to an increase in temperature [2]. The process is reversible during demagnetization. Usually, the isothermal magnetic entropy change ΔS_M or adiabatic temperature change ΔT_{ad} is utilized to estimate the magnitude of the magnetocaloric effect [3].

Magnetocaloric materials can be classified into first-order magnetic transition (FOMT) and second-order magnetic transition (SOMT) materials, according to the order of ferromagnetic (FM)–paramagnetic (PM) phase transition. FOMT material has a discontinuous magnetic transition process with temperature, which is usually related to the giant magnetocaloric effect (GMCE) [3]; however, narrow operating temperature span, high thermal and magnetic hysteresis, and inferior mechanical stability restrict its practical application. The mainly studied FOMT materials for near-room-temperature MR are $Gd_5(Si, Ge)_4$ alloys [4],

La(Fe, Si)$_{13}$ compounds [5], Mn-Fe-P-Si alloys [6], Heusler alloys [7], etc. In contrast, although the MCE of SOMT material is much lower, it usually possesses negligible magnetic hysteresis and nearly zero thermal hysteresis, which is beneficial for reducing energy losses in practical applications. Among the SOMT near-room-temperature refrigerants, Gd is the most representative as a reference material [8]. The high manufacturing cost and low corrosion resistance of Gd limit its practical application in near-room-temperature magnetic refrigeration technology [9].

Amorphous alloys with the unique atomic structure (short-range order and long-range disorder) belong to the SOMT material class in general and show excellent properties, such as neglectable magnetic and thermal hysteresis, tailorable Curie temperature, high mechanical properties and corrosion resistance, high resistivity (associated with low eddy current loss) and simple production process, which makes them good candidates as magnetic refrigerants [10]. Currently, studies on magnetocaloric amorphous alloys for the near-room-temperature region are mainly focused on Gd-based and Fe-based amorphous alloys. Although the Fe-based amorphous alloys have the advantages of suitable Curie temperature (T_C) and low cost of raw material, their MCE is generally not high enough; oppositely, many of the Gd-based amorphous alloys exhibit large MCE, but their T_C is far from room temperature [11].

It has been revealed that the T_C of Gd-Co binary amorphous alloys can be raised from 166 K to 282 K by increasing the amount of Co due to the enhancement of Co-Co exchange interaction [12–14]. Additionally, further increment in the transition metals (TM) content through replacing Gd with Fe or Ni can promote the T_C to 310 K; however, the clusters or nanocrystals will appear more easily in the alloy, weakening the magnetocaloric properties of the alloys [15,16]. If the concentration of Gd remains constant, minor substitution of Fe or Ni for Co will improve or diminish the T_C of Gd-Co amorphous alloys owing to the variation in interaction between the transition metals [17,18]. Meanwhile, the peak value of ΔS_M ($|\Delta S_M^{pk}|$) of the alloys nearly linearly depends on $T_C^{-2/3}$ [17,19]. However, in our previous work, it was found that excessive Fe replacement of Co results in a decrease in the T_C and $|\Delta S_M^{pk}|$ simultaneously [20], which may be ascribed to the enhancement of antiferromagnetic Gd-Fe exchange interactions and variation in predominant exchange interactions from ferrimagnetism to sperimagnetism [21,22].

On the basis of the molecular field theory (MFT), Gd-TM amorphous alloys can be constructed as a two-sublattice model, and three exchange interaction constants of J_{GdGd}, J_{TMTM} and $-J_{GdTM}$ (the positive and negative signs represent the ferromagnetic and antiferromagnetic exchange, respectively) can be derived by analyzing the temperature dependence of magnetization [23]. Particularly, in the Gd-Fe binary amorphous alloys, the change in Fe content causes the variation in magnetic transition behavior, which can be explained by the different exchange interaction constants [24]. Furthermore, Yano et al. reported that the addition of 10 at.% B in Gd$_{60}$Fe$_{40}$ amorphous alloy could manipulate the inversely bent (inflection-like) curve of the magnetization to the normal ferromagnetic curve, which is found to originate from the decrease in Fe magnetic moment and the enhancement of magnetic exchange constant $|J_{GdFe}|$ [25]. It has been demonstrated that co-doping of covalent B and Si modified the magnetic transition behavior and improved the magnetocaloric properties (with a larger $|\Delta S_M|$ at higher working temperature) of the amorphous (Gd$_{0.6}$Co$_{0.2}$Fe$_{0.2}$)$_{95}$B$_2$Si$_3$ alloy [26]. In this work, a series of Gd$_{54}$Fe$_{36}$B$_{10-x}$Si$_x$ (x = 0, 2, 5, 8, and 10) amorphous ribbons were prepared, and the influence of Si substitution for B on magnetic and magnetocaloric properties was investigated. In addition, to interpret the variation in magnetic and magnetocaloric properties with composition, the magnetic exchange interaction was analyzed based on the molecular field theory.

2. Experimental Details

Alloy ingots with nominal compositions of Gd$_{54}$Fe$_{36}$B$_{10-x}$Si$_x$ (x = 0, 2, 5, 8, 10) were prepared by arc-melting mixtures of high-purity Gd (99.95 wt%) and Fe (99.95 wt%) metals and pre-alloy BFe and SiFe (mass ratios of B/Fe and Si/Fe were 17.62/81.46 and 22.25/74.53,

respectively) under Ti-gettered argon atmosphere. Each ingot was overturned and remelted four times to ensure homogeneity. Then the as-spun ribbons were fabricated by single roller melt-spinning method with a copper wheel linear surface velocity of 50 m/s under a high-purity argon atmosphere. The structure of the as-spun ribbons was determined using an X-ray diffractometer (XRD, Bruker D8 Advance) in the 2θ range of $20°$–$80°$ with Cu K_α radiation ($\lambda = 0.154178$ nm). Thermal analyses of the samples were carried out using a differential scanning calorimeter (DSC, Netzsch STA499 F3) under the protection of an argon gas flow at a heating rate of 0.33 K/s. A physical property measurement system (PPMS, Quantum Design PPMS Evercool-II) was adopted to measure the temperature dependence of magnetization (*M-T*) curves under the external magnetic field of 10 Oe and 6 kOe. A superconducting quantum interference device (SQUID, Quantum Design MPMS 3) was utilized to detect the isothermal magnetization (*M-H*) curves under an applied field change of 0–20 kOe at various selected temperatures in the vicinity of the magnetic transition temperature (T_{tr}). All the magnetic properties were collected with the direction of the applied field parallel to the surface of the ribbons. To evaluate the magnetocaloric properties, the magnetic entropy change $|\Delta S_{\text{M}}|$ was calculated from the *M-H* curves using the Maxwell equation as follows [27]:

$$\Delta S_{\text{M}}(T, H) = S_{\text{M}}(T, H) - S_{\text{M}}(T, 0) = \int_0^H \left\{ \frac{\partial M(T, H)}{\partial T} \right\}_H \mathrm{d}H \tag{1}$$

which indicates that the magnetic entropy change $\Delta S_{\text{M}}(T,H)$ of a specific material is proportional to the derivative of magnetization with respect to temperature under a fixed field and to the magnetic field change. Typically, Equation (1) was numerically approximated as follows [6]:

$$\Delta S_{\text{M}}(T, H) = \sum_i \frac{M_i(T_{n+1}, H_i) - M_i(T_n, H_i)}{T_{n+1} - T_n} \delta H_i \tag{2}$$

where $M_i(T_{n+1}, H_i)$ and $M_i(T_n, H_i)$ are experimental values of magnetization at temperatures T_{n+1} and T_n under the applied field H_i, respectively.

3. Results and Discussion

3.1. Characterization of Amorphous Structure

Figure 1a shows the XRD patterns of the $Gd_{54}Fe_{36}B_{10-x}Si_x$ ($x = 0, 2, 5, 8, 10$) as-spun ribbons. Only one broad diffraction peak at around $2\theta = 33°$ without obvious peaks corresponding to the crystalline phase was obtained in each sample, which indicates the typical amorphous structure of the as-spun ribbons. The amorphous feature can be confirmed by the crystallization-related exothermic peaks in their DSC curves, as exhibited in Figure 1b, and the onset crystallization temperature (T_x) of $Gd_{54}Fe_{36}B_{10-x}Si_x$ amorphous alloys is 749, 762, 766, 743 and 686 K for $x = 0, 2, 5, 8$ and 10 respectively. With increasing content of Si, the T_x increases firstly and then decreases, implying that appropriate co-addition of Si and B effectively enhanced the thermal stability of amorphous $Gd_{54}Fe_{36}B_{10-x}Si_x$, while immoderate Si content ($x \geq 8$) induced the split of the exothermal peak and even two-step crystallization. There is no obvious glass transition in the DSC curves since the competing transformation to crystalline is predominant under the heating rate of 0.33 K/s [28]. For all the samples, the T_x is high enough to ensure the amorphous structure near room temperature.
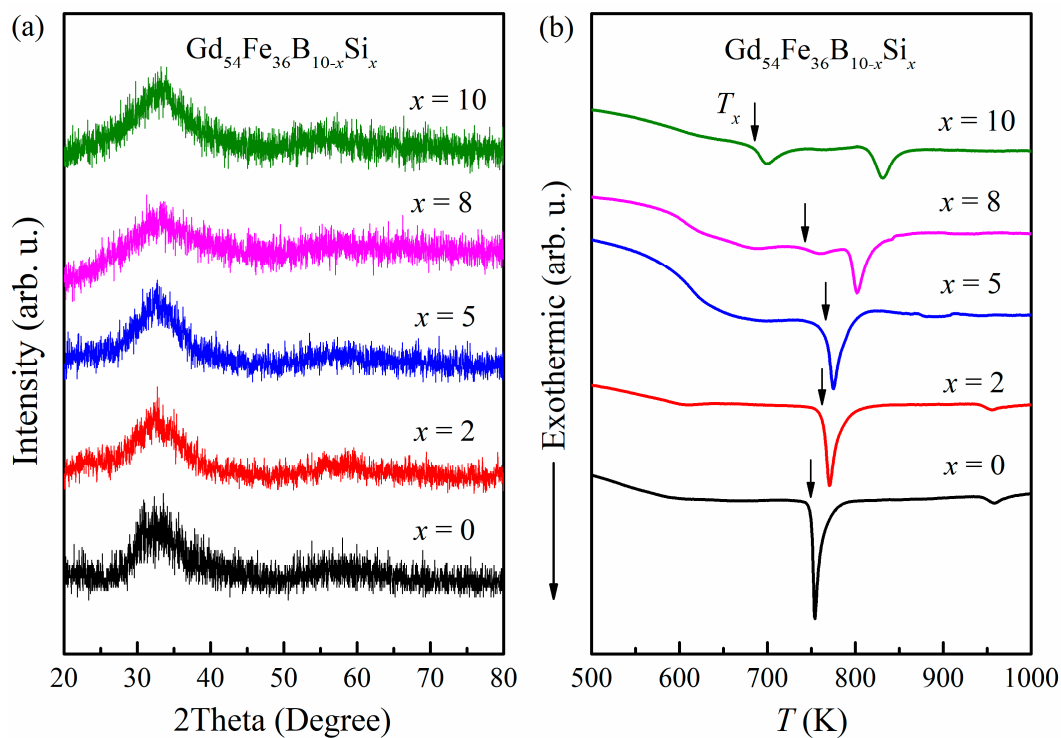
Figure 1. (**a**) XRD patterns and (**b**) DSC curves of the $Gd_{54}Fe_{36}B_{10-x}Si_x$ as-spun ribbons.

3.2. Determination of the Transition Temperature

Figure 2a shows the *M-T* curves of the $Gd_{54}Fe_{36}B_{10-x}Si_x$ amorphous ribbons measured under the applied field of 10 Oe. It can be seen that the magnetization reduced with rising temperature, presenting a ferrimagnetic–paramagnetic transition. The magnetic transition temperature T_{tr} was determined by the inflection-point method, taking the temperature corresponding to the minimum derivative of *M-T* curve (namely the dM/dT vs. *T* plot, displayed in the inset of Figure 2a). For the samples with $x = 0$, 2, 5, 8 and 10, the T_{tr} is 282, 296, 316, 342 and 364 K, respectively. As illustrated in Figure 2b, the T_{tr} increased nearly linearly with increasing Si content for the $Gd_{54}Fe_{36}B_{10-x}Si_x$ amorphous alloys, with the fitting expression of $T_{tr} = 8.1x + 279.7$, which is possibly due to the increase in magnetic exchange coupling [19,29,30]. Although only the concentration of non-magnetic B or Si elements changed, it may affect the magnetic moment and exchange interaction in the materials [25]. Similar results have been reported in amorphous alloys $Gd_{65}Fe_{10}Co_{10}Al_{10}X_5$ (X = B, Si) and $(Gd_{0.6}Co_{0.2}Fe_{0.2})_{95}B_xSi_{5-x}$ ($x = 0$, 2, 5) [26,31].

3.3. Magnetocaloric Properties

As indicated by Equation (1), the magnetic entropy change is approximately proportional to the dM/dT, and thereby the *M-H* isotherms of $Gd_{54}Fe_{36}B_{10-x}Si_x$ ($x = 0$, 2, 5, 8, 10) amorphous alloys at different temperatures near their individual T_{tr} were measured under a magnetic field changing from 0 to 20 kOe, as exhibited in Figure 3. The sweeping rate of the field was slow enough to ensure that the data were recorded in an isothermal process. The obvious magnetic transition process near the T_{tr} could be observed in all the samples except $Gd_{54}Fe_{36}Si_{10}$, which had not achieved a paramagnetic state at 385 K.
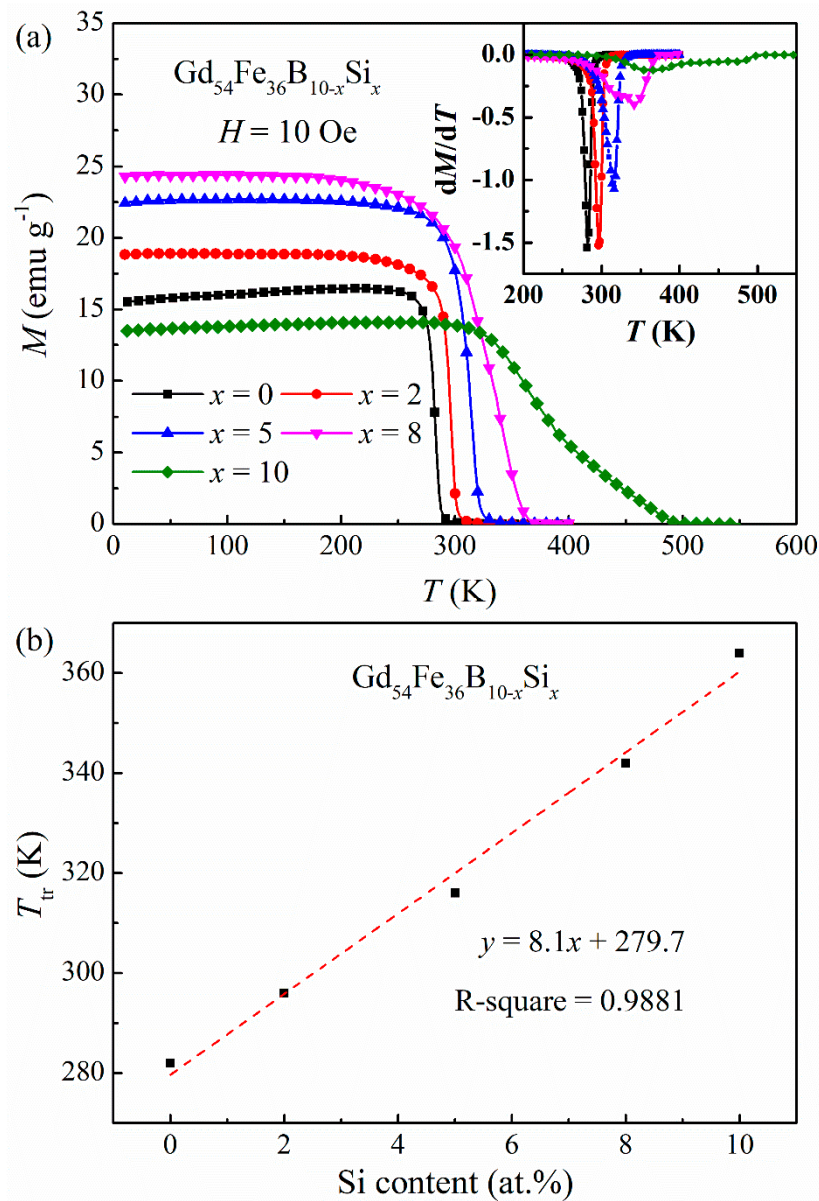
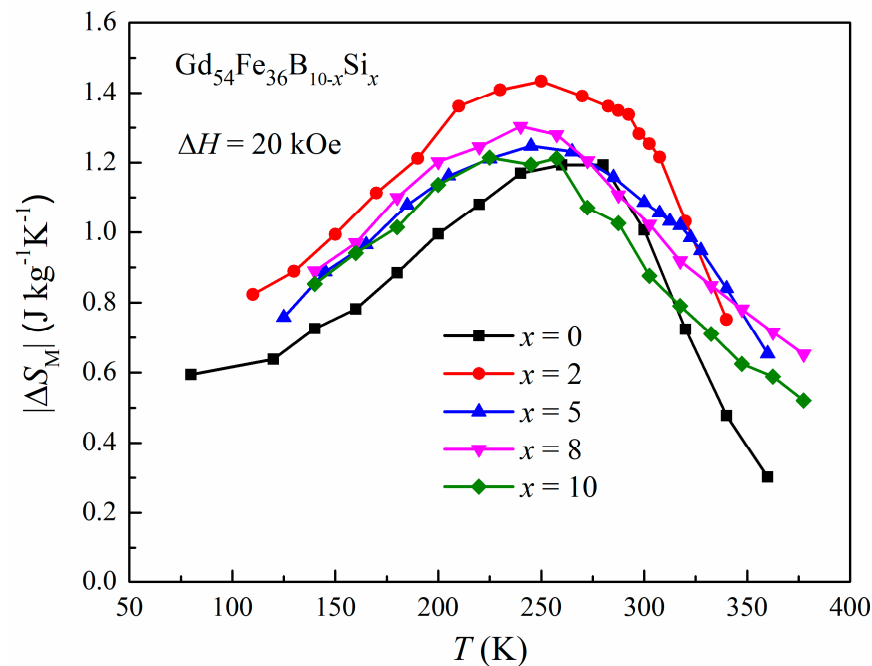**Figure 2.** (**a**) Temperature-dependent magnetization curves of $Gd_{54}Fe_{36}B_{10-x}Si_x$ amorphous ribbons under an applied field of 10 Oe. The inset presents the corresponding dM/dT-T plots. (**b**) Correlation between Si content and the T_C for $Gd_{54}Fe_{36}B_{10-x}Si_x$ amorphous alloys.

The magnetic entropy change as a function of temperature ($|\Delta S_M|$ vs. T curves) is displayed in Figure 4. The maximum magnetic entropy change ($|\Delta S_M^{pk}|$) of $Gd_{54}Fe_{36}B_{10-x}Si_x$ amorphous alloys under field change of 20 kOe is 1.20, 1.43, 1.25, 1.30 and 1.21 J kg^{-1}K^{-1} at 260, 250, 245, 240 and 225 K for x = 0, 2, 5, 8 and 10, respectively, which increases firstly and then decreases with increasing content of Si, showing a nonlinear correlation. $Gd_{54}Fe_{36}B_8Si_2$ possesses the highest $|\Delta S_M^{pk}|$. In our previous study, a similar phenomenon was observed in the $(Gd_{0.6}Co_{0.2}Fe_{0.2})_{95}B_xSi_{5-x}$ (x = 0, 2, 5) series of amorphous alloys [26]. The relative cooling power (*RCP*) is another parameter for estimating the MCE and energy efficiency of a magnetic refrigerant, and it can be evaluated by the product $RCP = \left|\Delta S_M^{pk}\right| \times \Delta T_{FWHM}$, where the ΔT_{FWHM} is the full width at half maximum of the entropy curve [32]. In this work, the values of *RCP* for the amorphous $Gd_{54}Fe_{36}B_{10-x}Si_x$ with x = 0, 2, 5, 8 and 10 are 295, 374, 323, 362 and 321 J kg^{-1} (under the field change of 0–20 kOe), respectively. Owing to the larger value of $|\Delta S_M^{pk}|$, the $Gd_{54}Fe_{36}B_8Si_2$ shows the highest *RCP*. Compared with the magnetocaloric properties (including $|\Delta S_M^{pk}|$ and *RCP*) of some other materials (with

similar working temperature) listed in Table 1, the *RCP* values of the presently studied materials are higher in spite of their lower $|\Delta S_M^{pk}|$, which results from the broadened entropy curve and larger ΔT_{FWHM}. This is the typical characteristic of MCE obtained in Gd-based amorphous alloys with the second-order magnetic transition (SOMT) [18,19,29,30,33,34]. The Arrott plots (M^2 vs. H/M) of Gd$_{54}$Fe$_{36}$B$_{10-x}$Si$_x$ ribbons were derived from the *M-H* isotherms, as shown in Figure 5. According to Banerjee criteria [35], the slopes of the Arrott plots are positive in the whole temperature range for all the samples, indicating that their magnetic transition is SOMT.
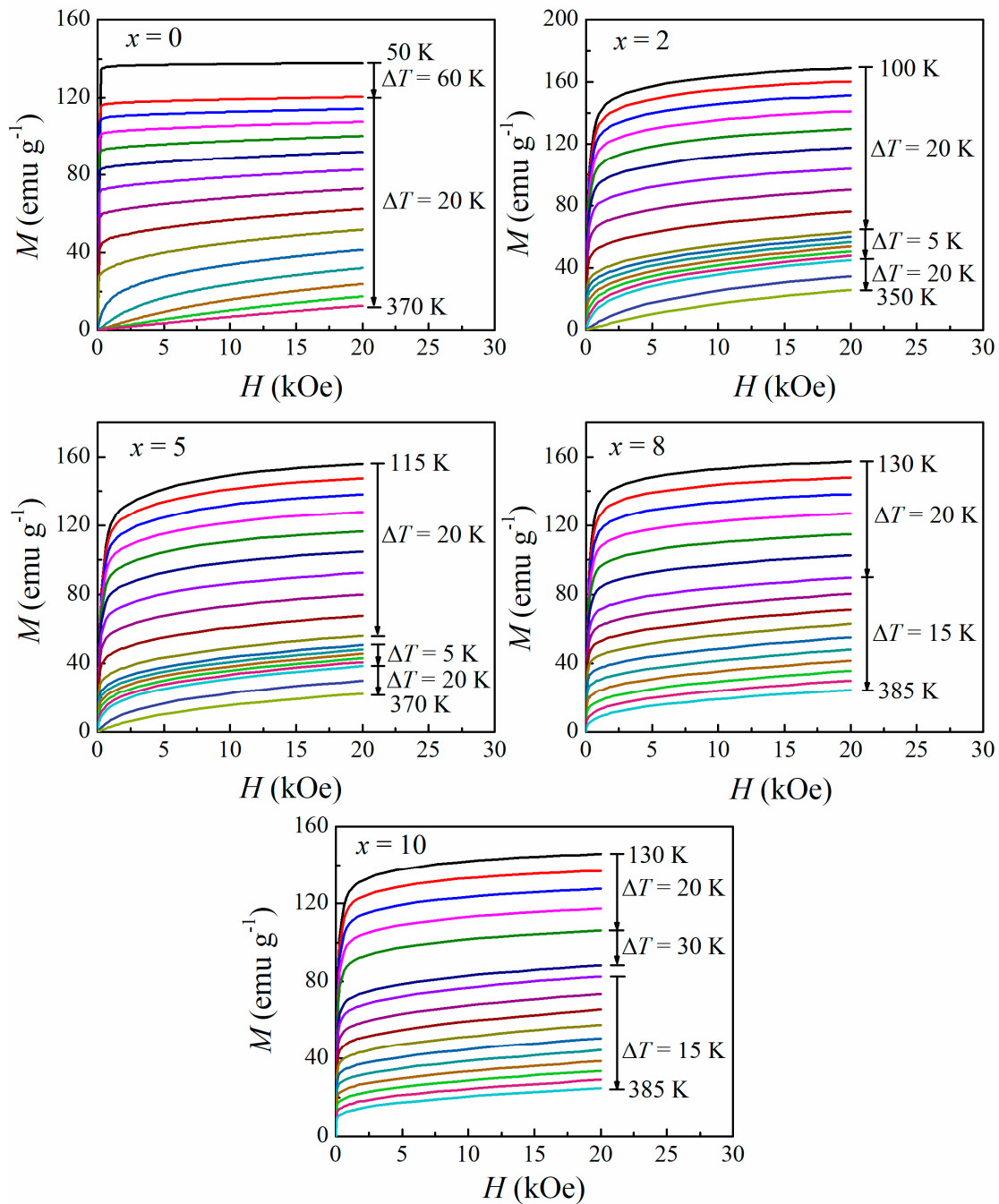
Figure 3. Isothermal magnetization curves of Gd$_{54}$Fe$_{36}$B$_{10-x}$Si$_x$ amorphous ribbons near their T_C under the field changing from 0 to 20 kOe.

Figure 4. Temperature dependence of the $|\Delta S_\mathrm{M}|$ for $Gd_{54}Fe_{36}B_{10-x}Si_x$ amorphous alloys under the magnetic field change of 20 kOe.

However, the *RCP* is now recognized to overestimate the actual refrigerating capacity of the materials with a minor magnetic entropy change in an unreasonably broad temperature range [32]. In this regard, the temperature average entropy change (*TEC*) was introduced as a reliable figure of merit to assess the magnetocaloric efficiency; it is calculated by the following equation [36]:

$$TEC(\Delta T_{lift}) = \frac{1}{\Delta T_{lift}} \max \int_{T_{\mathrm{mid}}+\frac{\Delta T_{lift}}{2}}^{T_{\mathrm{mid}}-\frac{\Delta T_{lift}}{2}} |\Delta S_\mathrm{M}(T)| dT \tag{3}$$

where ΔT_{lift} is the desired lift temperature of the device and T_{mid} is the central temperature that maximizes the $TEC(\Delta T_{lift})$ value for a given ΔT_{lift}. In this research, the ΔT_{lift} was chosen between 10 K and 100 K with an interval of 10 K, and Figure 6a illustrates the variation in *TEC* values with respect to ΔT_{lift} in the magnetic field change of 20 kOe for the $Gd_{54}Fe_{36}B_{10-x}Si_x$ amorphous alloys. The correlation between *TEC* and the content of Si indicates that the partial replacement of B by Si improves the magnetocaloric performances in this series of materials, as reflected by the changing tendency of $|\Delta S_\mathrm{M}|$. Additionally, the *TEC* values gradually decrease with increasing ΔT_{lift} for each sample, and similar behavior has been reported previously [6,37,38]. It should be noted that the *TEC* changes very gently with the different ΔT_{lift} values, which is ascribed to the table-like $|\Delta S_\mathrm{M}|(T)$ curves (the $|\Delta S_\mathrm{M}|$ retains almost constant in a wide temperature range). As revealed in Figure 6b, the *TEC*(30 K) and $|\Delta S_\mathrm{M}^{\mathrm{pk}}|$ of amorphous $Gd_{54}Fe_{36}B_8Si_2$ display a similar ΔH dependence, and their values are very close at any magnetic field, demonstrating less loss in the material during the magnetic transition. The obtained *TEC*(30 K, 20 kOe) and *TEC*(30 K, 15 kOe) values of $Gd_{54}Fe_{36}B_8Si_2$ are 1.42 J kg^{-1}K^{-1} and 1.07 J kg^{-1}K^{-1}, respectively. Compared with some other materials, the values are lower than those of Gd (*TEC*(10 K, 10 kOe) = 2.91 J kg^{-1}K^{-1}) [36] but comparable to those of $(La_{0.7}Pr_{0.3})_{0.8}Sr_{0.2}Mn_{0.9}Co_{0.1}O_{3\pm\delta}$ (*TEC*(10 K, 20 kOe) = 1.3 J kg^{-1}K^{-1}) [39] and $La_{0.65}Nd_{0.05}Ba_{0.3}Mn_{0.85}Cr_{0.15}O_3$ (*TEC*(25 K, 20 kOe) = 1.7 J kg^{-1}K^{-1}) [38] and higher than those of $Fe_{63.5}Cr_{10}Si_{13.5}B_9Nb_3Cu_1$ amorphous alloy (*TEC*(10 K, 15 kOe) = 0.83 J kg^{-1}K^{-1}) [36,38–40]. Although the magnetocaloric performance estimated by *TEC* is

not very good, the table-like MCE with a wide temperature range was observed in all the samples, enabling them to be more suitable for the Ericsson thermodynamic cycle [32].
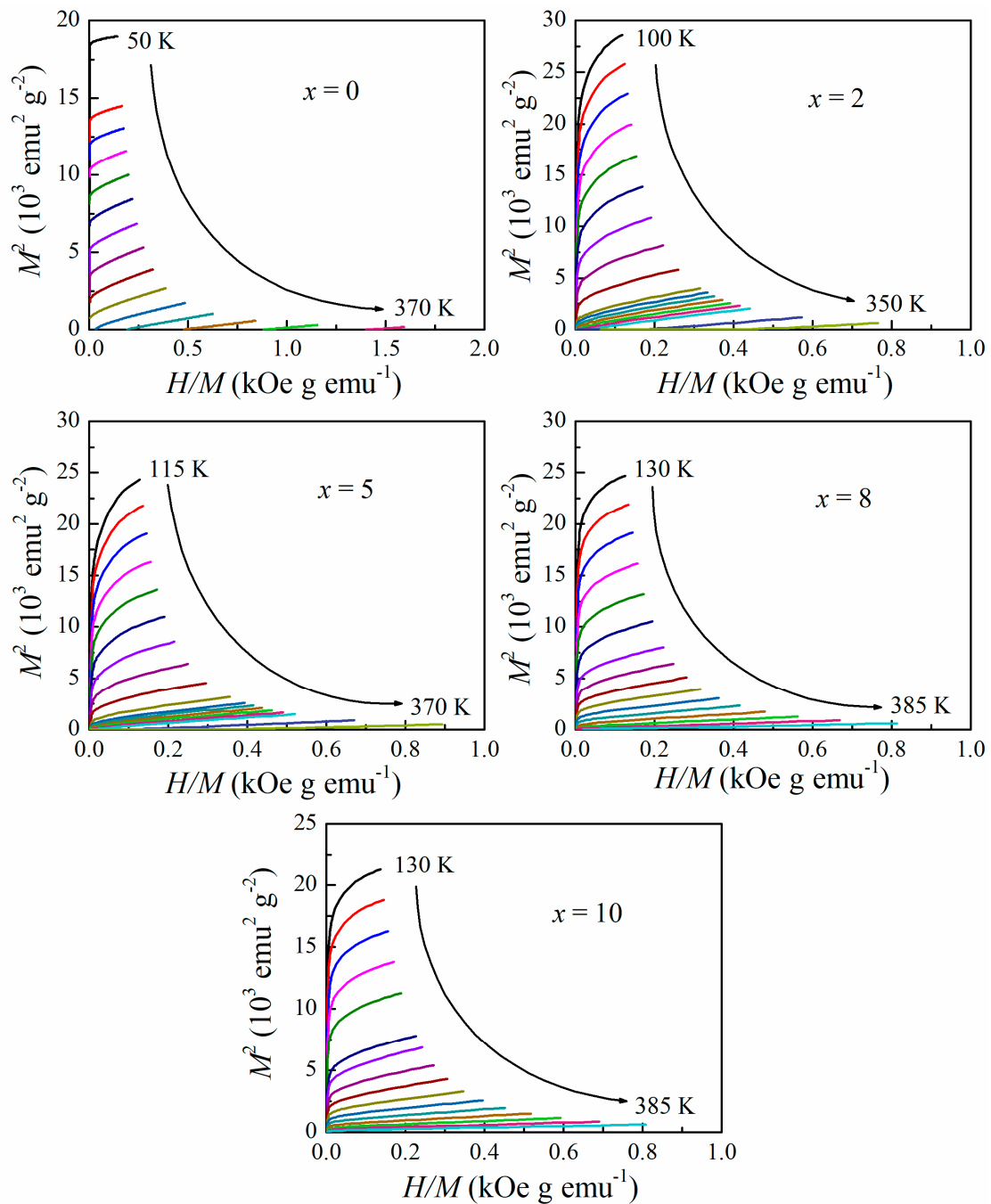
Figure 5. Arrott plots of amorphous $Gd_{54}Fe_{36}B_{10-x}Si_x$ ribbons.
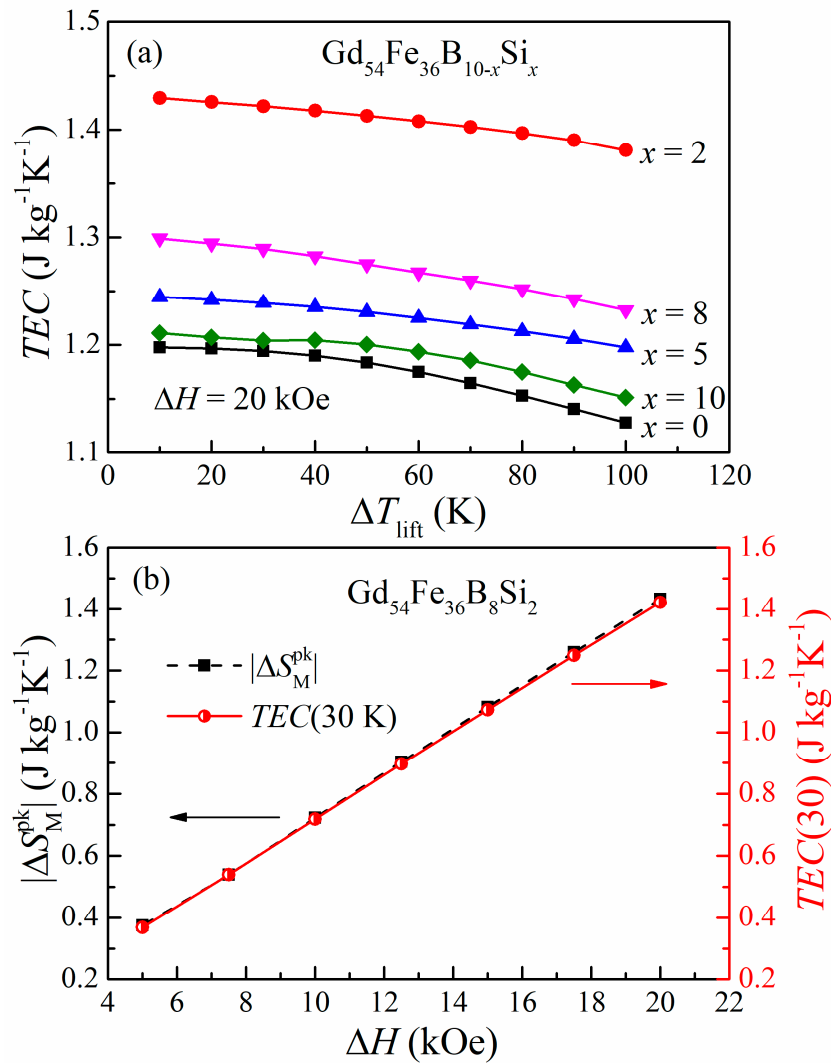
Figure 6. (a) *TEC* as a function of ΔT_{lift} for the $Gd_{54}Fe_{36}B_{10-x}Si_x$ amorphous alloys, under the field change of 0–20 kOe. (b) Magnetic field dependence of the *TEC*(30 K) and $|\Delta S_M^{pk}|$ for amorphous $Gd_{54}Fe_{36}B_8Si_2$.

Table 1. Magnetocaloric properties (the magnetic transition temperature T_{tr}, maximum magnetic entropy change $|\Delta S_M^{pk}|$ and its corresponding temperature T_{pk} and relative cooling power *RCP*) of amorphized $Gd_{54}Fe_{36}B_{10-x}Si_x$ ribbons and some other materials in comparison. The A and C denote the amorphous and crystalline states, respectively.

| Alloys	Structure	T_{tr} (K)	T_{pk} (K)	$\|\Delta S_M^{pk}\|$ (J kg^{-1}K^{-1})	*RCP* (J kg^{-1})	Ref.
		H = 10 Oe		ΔH = 20 kOe		
$Gd_{54}Fe_{36}B_{10}$	A	282	260	1.20	295	This work
$Gd_{54}Fe_{36}B_8Si_2$	A	296	250	1.43	374	This work
$Gd_{54}Fe_{36}B_5Si_5$	A	316	245	1.25	323	This work
$Gd_{54}Fe_{36}B_2Si_8$	A	342	240	1.30	362	This work
$Gd_{54}Fe_{36}Si_{10}$	A	364	225	1.21	321	This work
$Gd_{50}Co_{50}$	A	267.2	~267	2.36	212.8	[33]
$Gd_{55}Co_{35}Fe_{10}$	A	268	~268	1.72	337	[34]
$Gd_{50}Fe_{45}Co_5$	A	289.5	288.5	1.85	289	[18]
Gd	C	292	~295	5.2	226.9	[9,41]
$Gd_5Si_2Ge_2$	C	276	~276	18.4	195.3	[4,9]
$LaFe_{11.05}Co_{0.91}Si_{1.04}$	C	282.1	~282	10.5	168.7	[5,9]
$LaFe_{11.40}Co_{0.52}Si_{1.09}$	C	237.7	~238	16.8	147.4	[5,9]

3.4. Magnetic Exchange Interaction

In Figure 2, it can be found that the ferrimagnetic–paramagnetic magnetic transition process becomes broad and gentle with increasing Si content, which is possibly attributed to the variation in Fe magnetic moment and magnetic exchange constant (J_{GdGd}, J_{GdFe}, J_{FeFe}) induced by the replacement of B with Si [25,42]. Additionally, the T_{tr} obtained in the low magnetic field of 10 Oe is higher than the T_{pk} achieved under the high magnetic field of 20 kOe, while the T_{tr} is similar to the T_{pk} for the other series of alloys, as displayed in Table 1. Especially for the present Si-containing $Gd_{54}Fe_{36}B_{10-x}Si_x$ amorphous samples, the discrepancy between T_{tr} and T_{pk} becomes larger with increasing content of Si, and this may be caused by the varied antiferromagnetic coupling between Fe and Gd sublattices associated with the composition and magnetic field [24,25].

To investigate the origin of these phenomena in detail, an MFT analysis was carried out with the two-sublattice model [43]. First of all, the *M-T* curves of $Gd_{54}Fe_{36}B_{10-x}Si_x$ amorphous ribbons were measured under the magnetic field of 6 kOe, which ensures the saturation state of the samples, as exhibited in Figure 7 (open circle). The inflection-like behavior with the characteristic of an inversely bent curve in a relatively wide temperature range can be observed for $x = 8$ and 10, similar to the transition type revealed in Gd-rich region Gd-Fe amorphous ribbons [25]. In the next step, each sublattice magnetization M_{Gd} and M_{Fe} and the total magnetization *M* were calculated by assigning some values to three exchange integration constants, J_{GdGd}, J_{GdFe} and J_{FeFe}, at a certain temperature *T*, then the *M-T* curves in the field of 6 kOe was fitted through adopting the nonlinear least square method [44]. The ferrimagnetic model was constructed with the following parameters: The Landé factors of Gd and Fe are $g_{Gd} = g_{Fe} = 2$. The coordination number Z_{ij} (i, j = Gd, Fe) is expressed as $Z_{GdGd} = Z_{FeGd} = 7.2$ ($= \frac{12X_{Gd}}{X_{Gd}+X_{Fe}}$) and $Z_{GdFe} = Z_{FeFe} = 4.8$ ($= \frac{12X_{Fe}}{X_{Gd}+X_{Fe}}$), where X_{Fe} and X_{Gd} are atomic content of Fe and Gd respectively. The spin quantum number S_{Gd} is 7/2 for the Gd sublattice, while the S_{Fe} was derived from Fe magnetic moment μ_{Fe} ($\mu_{Fe} = g_{Fe}S_{Fe}$), and μ_{Fe} was evaluated from the magnetization μ_a at 10 K under 6 kOe by $\mu_a = |X_{Gd}\mu_{Gd} - X_{Fe}\mu_{Fe}|/100$ (where $\mu_{Gd} = g_{Gd}S_{Gd} = 7\ \mu_B$) [45]. As a result, the J_{GdGd}, J_{GdFe} and J_{FeFe} were derived, and the fitting profiles of M_{Gd}, M_{Fe} and *M* are depicted in Figure 7 (solid line). It can be seen that all the calculated results are in good accordance with the experimental data.

The content dependence of μ_{Fe}, J_{GdGd}, $-J_{GdFe}$, J_{FeFe}, the $-J_{GdFe}/J_{FeFe}$ ratio and $|\Delta S_M^{pk}|$ for $Gd_{54}Fe_{36}B_{10-x}Si_x$ amorphous alloys is displayed in Figure 8. The μ_{Fe} increases from 1.60 μ_B (for $x = 0$) to 2.68 μ_B (for $x = 2$) first and then decreases to 1.4 μ_B (for $x = 10$). Similar results can be found in amorphous alloys $Fe_{56}Gd_{24}Si_{12}B_8$ ($\mu_{Fe} \approx 1.40\ \mu_B$) and $Fe_{56}Gd_{24}B_{20}$ ($\mu_{Fe} = 1.22\ \mu_B$) [45,46]. On one side, compared with the B element, Si possesses more covalent electrons (mainly 3p electrons), which possibly intensifies the transfer of electrons to the 3d orbital of Fe, leading to the lower value of μ_{Fe} [25,46,47]. On the other side, the substitution of Si for B could change the local environment and affect the magnetic moment of Fe atoms [48]. In this study, for the moderate Si content, B may absorb electrons from Fe atoms and promote μ_{Fe} [49]; for the alloys with high content of Si or B ($x = 0$ and 10), the p-d hybridization dominates the reduction in μ_{Fe} [50].

With the replacement of B by Si in amorphous $Gd_{54}Fe_{36}B_{10-x}Si_x$ alloys, the J_{GdGd} increases slightly, reflecting the decrease in the average distance between Gd atoms [24], which is probably attributed to the stronger atomic interaction between Fe and Si (in comparison with the Fe-B pairs), and more metalloid atoms tend to surround Fe atoms [51]. Furthermore, after the addition of Si, fewer B atoms appear at the nearest neighbor locations around Fe atoms, and as described above, B absorbs electrons from Fe for the lower B content [52].
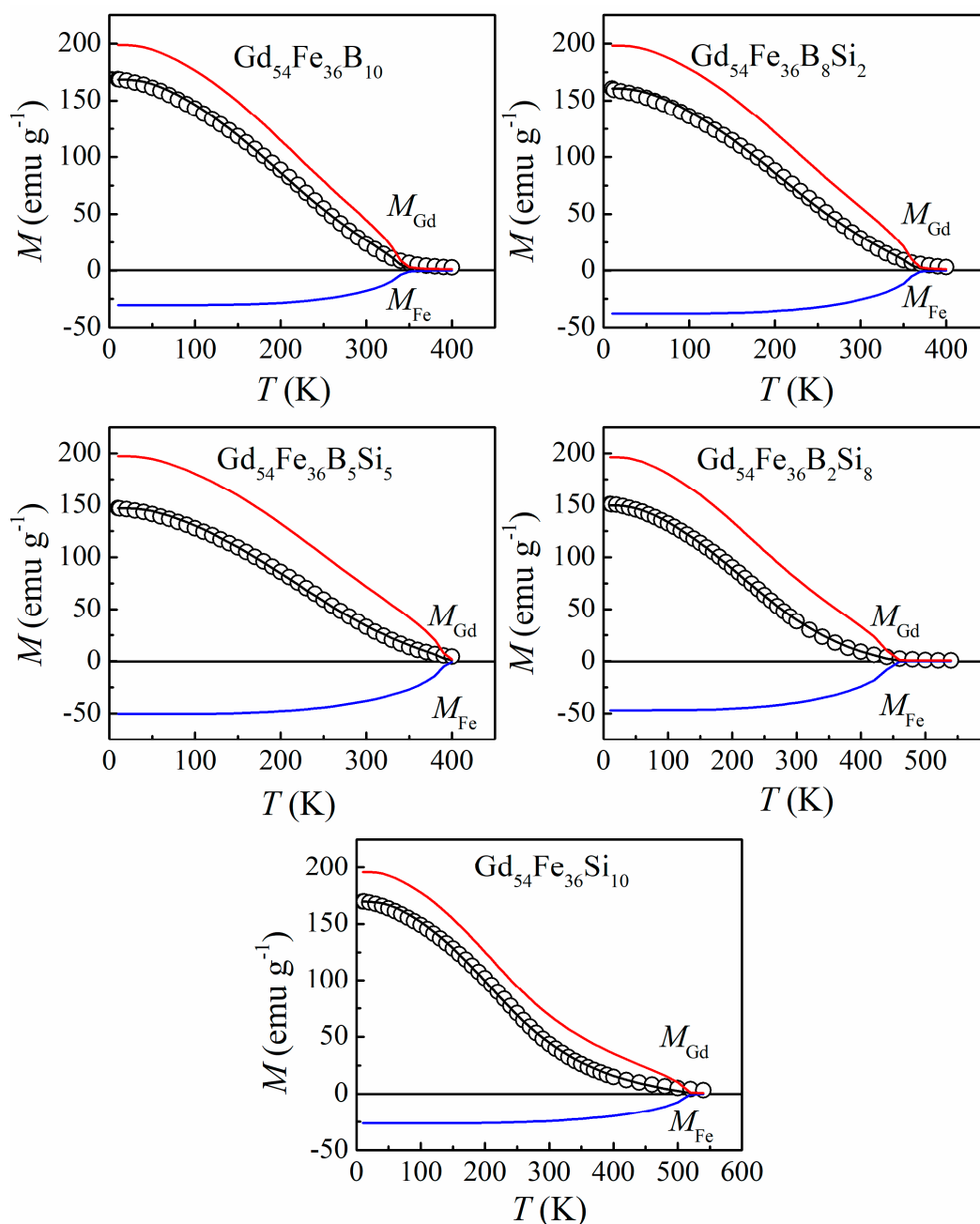
Figure 7. *M-T* curves for the $Gd_{54}Fe_{36}B_{10-x}Si_x$ (x = 0, 2, 5, 8, 10) amorphous alloys under magnetic field of 6 kOe (open circles) and the fitting results (solid line). Calculated data of two sublattice magnetizations (M_{Gd} and M_{Fe} are denoted as "red line" and "blue line", respectively) are also shown.

It can be seen that the introduction of Si has stronger impacts on $-J_{GdFe}$ and J_{FeFe} than on J_{GdGd}. Additionally, both $-J_{GdFe}$ and J_{FeFe} decrease firstly and then increase with increasing Si content; the variation rule is opposite to that of μ_{Fe}, as displayed in Figure 8. The overlap between 5d electron wave-functions of Gd and 3d electron wave-functions of Fe is considered to be the origin of the antiferromagnetic exchange coupling $-J_{GdFe}$ [53]; therefore, the lost 3d electron of Fe absorbed by the surrounding B (with moderate content of Si, i.e., x = 2, 5 and 8) is in accordance with the weakened 3d–5d interaction [25]. The effect of B addition on J_{FeFe} in the amorphous $Gd_{54}Fe_{36}B_{10}$ alloys is neglectable [25], which can be interpreted by its statistically random distribution in the structure [24]. However, Si has a stronger atomic interaction with Fe and then preferentially neighbors Fe, resulting in the deviation from the statistical distribution, which is reflected by the great increase

in exchange constant J_{FeFe} in the $Gd_{54}Fe_{36}Si_{10}$ [24]. For the $Gd_{54}Fe_{36}B_{10-x}Si_x$ samples, partial replacement of B by Si may reduce the distance between Fe atoms, and the exchange interaction decreases according to the Bethe–Slater curve [54].
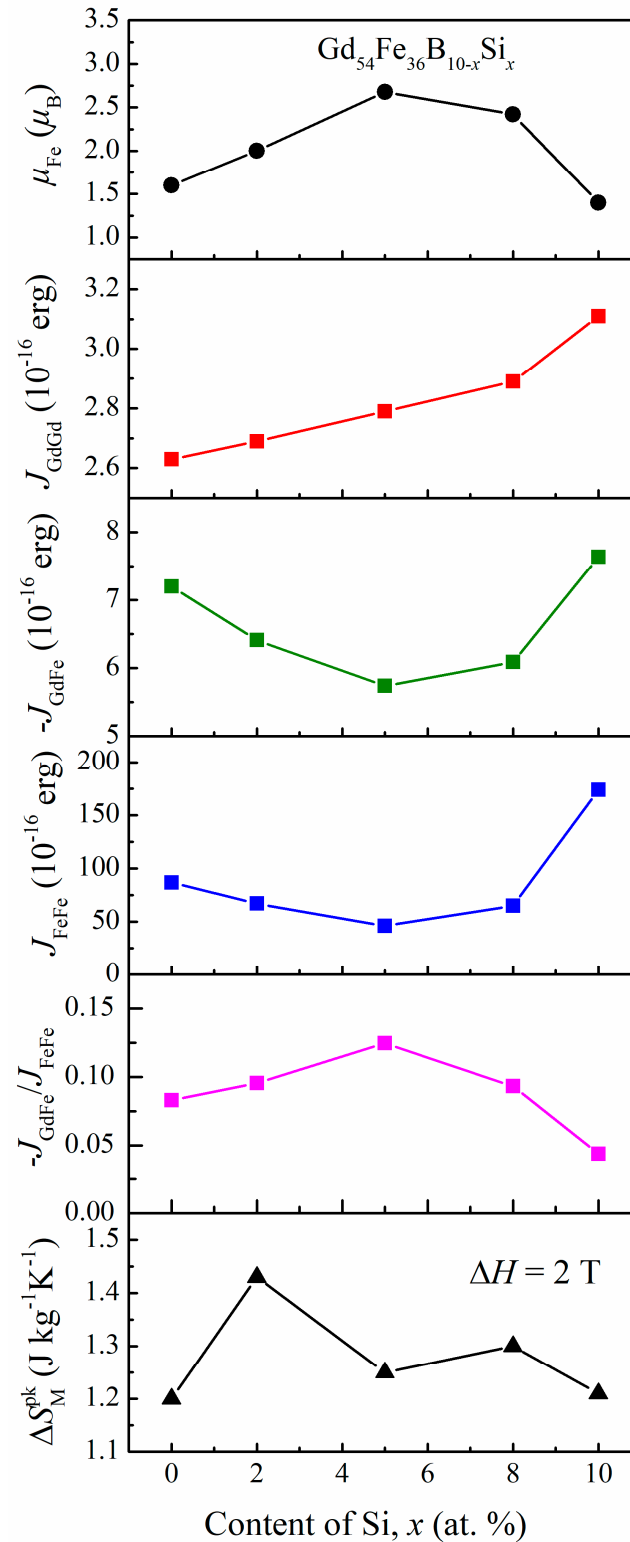
Figure 8. Correlation of magnetic moment of Fe, exchange interaction constants J_{GdGd}, $-J_{GdFe}$ and J_{FeFe}, ratio of $-J_{GdFe}/J_{FeFe}$, and $|\Delta S_M^{pk}|$ with the content of Si for amorphous $Gd_{54}Fe_{36}B_{10-x}Si_x$. The sign of J_{GdGd} and J_{FeFe} is positive but J_{GdFe} is negative.

It has been reported that the inflection-like magnetic transition of a Gd-TM amorphous alloy can be adjusted to normal ferromagnetic–paramagnetic transition by increasing the ratio of $-J_{\text{GdTM}}/J_{\text{TMTM}}$ when the J_{GdGd} remains constant [55]. As shown in Figure 8, the value of $-J_{\text{GdFe}}/J_{\text{FeFe}}$ increases first and then decreases with Si content rising from 0 to 10, which can explain the inflection-like *M-T* curves observed for $\text{Gd}_{54}\text{Fe}_{36}\text{B}_{10-x}\text{Si}_x$ amorphous alloys with $x = 8$ and 10. Moreover, adding more Si probably makes the atomic structure deviate from the statistical distribution, which leads to compositional fluctuation or localized heterogeneity [24]; then the larger discrepancy between T_{tr} and T_{pk} was obtained [56].

In Figure 8, the variation tendency of $-J_{\text{GdFe}}/J_{\text{FeFe}}$ and $|\Delta S_M{}^{\text{pk}}|$ with Si content is similar, except for the $\text{Gd}_{54}\text{Fe}_{36}\text{B}_5\text{Si}_5$; the atomic-scale structure and accurate μ_{Fe} of this series of alloys need to be clarified further. Nevertheless, it can be revealed that the appropriate substitution of Si for B promotes the value of $|\Delta S_M{}^{\text{pk}}|$ and table-like MCE of amorphous $\text{Gd}_{54}\text{Fe}_{36}\text{B}_{10-x}\text{Si}_x$ alloys; this can be attributed to the enhancement of the $-J_{\text{GdFe}}/J_{\text{FeFe}}$ and modified magnetic transition behavior. An excessive amount of Si results in a decline in the $-J_{\text{GdFe}}/J_{\text{FeFe}}$, an inflection-like transition and the deterioration of magnetocaloric properties.

4. Conclusions

In summary, the effect of Si substitution for B on thermal stability, magnetic transition behavior and magnetocaloric properties of melt-spun $\text{Gd}_{54}\text{Fe}_{36}\text{B}_{10-x}\text{Si}_x$ ($x = 0$, 2, 5, 8, 10) amorphous alloys was researched. With appropriate content of Si, the alloys showed enhanced thermal stability and broadened table-like MCE; with excessive Si, the alloys exhibited poorer thermal stability, inflection-like transition behavior and weakened MCE. Among present alloys, $\text{Gd}_{54}\text{Fe}_{36}\text{B}_8\text{Si}_2$ possesses the largest values of $|\Delta S_M{}^{\text{pk}}|$ (1.43 J kg^{-1}K^{-1}), *RCP* (374 J kg^{-1}) and *TEC*(30 K) (1.42 J kg^{-1}K^{-1}) under an applied field of 20 kOe, as well as a table-like MCE, which makes it more suitable for the MR with the Ericsson cycle.

The variation in magnetic exchange constants J_{GdGd}, J_{GdFe} and J_{FeFe} was obtained by fitting the temperature dependence of magnetization according to the molecular field theory and two-sublattice model. Substitution of B with Si induces the different ways of electron transfer and different atomic interaction (Fe-Si pairs are stronger than Fe-B), resulting in the nonlinear correlation between μ_{Fe}, J_{GdGd}, $-J_{\text{GdFe}}$, J_{FeFe} and $-J_{\text{GdFe}}/J_{\text{FeFe}}$ and Si content. Therefore, the shape of the magnetic transition curve and the magnetocaloric properties changed nonlinearly.

Author Contributions: Conceptualization, H.Z.; Methodology, H.Z.; Validation, H.Z. and J.T.; Formal analysis, H.Z., J.T. and H.L.; Investigation, H.Z., J.T., X.Z. and H.S.; Resources, H.Z.; Data curation, H.Z., J.T. and J.Y.; Writing—original draft, J.T.; Writing—review & editing, H.Z. and H.L.; Visualization, H.Z., J.T., X.Z., J.Y., H.S., Y.Z. and W.C.; Supervision, H.Z.; Project administration, H.Z., W.L. and A.X.; Funding acquisition, W.L. and A.X. All authors have read and agreed to the published version of the manuscript.

Data Availability Statement: The data presented in this study are available on request from the corresponding author.

References

1. Balli, M.; Jandl, S.; Fournier, P.; Kedous-Lebouc, A. Advanced materials for magnetic cooling: Fundamentals and practical aspects. *Appl. Phys. Rev.* **2017**, *4*, 021305. [CrossRef]
2. Pecharsky, V.K.; Gschneidner, K.A. Advanced magnetocaloric materials: What does the future hold? *Int. J. Refrig.* **2006**, *29*, 1239–1249. [CrossRef]
3. Taguchi, Y.; Sakai, H.; Choudhury, D. Magnetocaloric Materials with Multiple Instabilities. *Adv. Mater.* **2017**, *29*, 1606144. [CrossRef] [PubMed]
4. Pecharsky, V.K.; Gschneidner, K.A., Jr. Giant Magnetocaloric Effect in $Gd_5(Si_2Ge_2)$. *Phys. Rev. Lett.* **1997**, *78*, 4494–4497. [CrossRef]
5. Skokov, K.P.; Karpenkov, A.Y.; Karpenkov, D.Y.; Gutfleisch, O. The maximal cooling power of magnetic and thermoelectric refrigerators with $La(FeCoSi)_{13}$ alloys. *J. Appl. Phys.* **2013**, *113*, 17A945. [CrossRef]
6. Zheng, Z.G.; Wang, H.Y.; Li, C.F.; Chen, X.L.; Zeng, D.C.; Yuan, S.F. Enhancement of Magnetic Properties and Magnetocaloric Effects for $Mn_{0.975}Fe_{0.975}P_{0.5}Si_{0.5}$ Alloys by Optimizing Quenching Temperature. *Adv. Eng. Mater.* **2022**, *25*, 2200160. [CrossRef]
7. Liu, J.; Gottschall, T.; Skokov, K.P.; Moore, J.D.; Gutfleisch, O. Giant magnetocaloric effect driven by structural transitions. *Nat. Mater.* **2012**, *11*, 620–626. [CrossRef]
8. Kitanovski, A. Energy Applications of Magnetocaloric Materials. *Adv. Energy. Mater.* **2020**, *10*, 7. [CrossRef]
9. Gottschall, T.; Skokov, K.P.; Fries, M.; Taubel, A.; Radulov, I.; Scheibel, F.; Benke, D.; Riegg, S.; Gutfleisch, O. Making a cool choice: The materials library of magnetic refrigeration. *Adv. Eng. Mater.* **2019**, *9*, 1901322. [CrossRef]
10. Luo, Q.; Wang, W.H. Magnetocaloric effect in rare earth-based bulk metallic glasses. *J. Alloys Compd.* **2010**, *495*, 209–216. [CrossRef]
11. Tang, B.Z.; Guo, D.Q.; Ding, D.; Xia, L.; Chan, K.C. Large adiabatic temperature rise above the water ice point of a minor Fe substituted $Gd_{50}Co_{50}$ amorphous alloy. *J. Non-Cryst. Solids* **2017**, *464*, 30–33. [CrossRef]
12. Wang, Z.W.; Yu, P.; Cui, Y.T.; Xia, L. Near room temperature magneto-caloric effect of a $Gd_{48}Co_{52}$ amorphous alloy. *J. Alloys Compd.* **2016**, *658*, 598–602. [CrossRef]
13. Wu, C.; Ding, D.; Xia, L.; Chan, K.C. Achieving tailorable magneto-caloric effect in the Gd-Co binary amorphous alloys. *AIP Adv.* **2016**, *6*, 035302. [CrossRef]
14. Zhang, C.L.; Wang, D.H.; Han, Z.D.; Xuan, H.C.; Gu, B.X.; Du, Y.W. Large magnetic entropy changes in Gd-Co amorphous ribbons. *J. Appl. Phys.* **2009**, *105*, 013912. [CrossRef]
15. Tang, B.; Xie, H.; Li, D.; Xia, L.; Yu, P. Microstructure and its effect on magnetic and magnetocaloric properties of the $Co_{50}Gd_{50-x}Fe_x$ glassy ribbons. *J. Non-Cryst. Solids* **2020**, *533*, 119935. [CrossRef]
16. Wang, X.; Tang, B.; Wang, Q.; Yu, P.; Ding, D.; Xia, L. $Co_{50}Gd_{48-x}Fe_2Ni_x$ amorphous alloys with high adiabatic temperature rise near the hot end of a domestic magnetic refrigerator. *J. Non-Cryst. Solids* **2020**, *544*, 120146. [CrossRef]
17. Song, M.; Huang, L.; Tang, B.; Ding, D.; Zhou, Q.; Xia, L. Enhanced Curie temperature and magnetic entropy change of $Gd_{50}Co_{50-x}Ni_x$ amorphous alloys. *Mod. Phys. Lett. B* **2020**, *34*, 2050050. [CrossRef]
18. Liu, G.L.; Zhao, D.Q.; Bai, H.Y.; Wang, W.H.; Pan, M.X. Room temperature table-like magnetocaloric effect in amorphous $Gd_{50}Co_{45}Fe_5$ ribbon. *J. Phys. D Appl. Phys.* **2016**, *49*, 055004. [CrossRef]
19. Zhang, Z.; Tang, Q.; Wang, F.; Zhang, H.; Zhou, Y.; Xia, A.; Li, H.; Chen, S.; Li, W. Tailorable magnetocaloric effect by Fe substitution in Gd-(Co, Fe) amorphous alloy. *Intermetallics* **2019**, *111*, 106500. [CrossRef]
20. Zhang, H.Y.; Ouyang, J.T.; Ding, D.; Li, H.L.; Wang, J.G.; Li, W.H. Influence of Fe substitution on thermal stability and magnetocaloric effect of $Gd_{60}Co_{40-x}Fe_x$ amorphous alloy. *J. Alloys Compd.* **2018**, *769*, 186–192. [CrossRef]
21. Liu, X.Y.; Barclay, J.A.; Gopal, R.B.; Földeàki, M.; Chahine, R.; Bose, T.K.; Schurer, P.J.; LaCombe, J.L. Thermomagnetic properties of amorphous rare-earth alloys with Fe, Ni, or Co. *J. Appl. Phys.* **1996**, *79*, 1630–1641. [CrossRef]
22. Elkenany, M.M.; Aly, S.H.; Yehia, S. Magnetothermal properties and magnetocaloric effect in transition Metal-Rich Gd-Co and Gd-Fe amorphous alloys. *Cryogenics* **2022**, *123*, 103439. [CrossRef]
23. Hansen, P. Magnetic amorphous alloys. In *Handbook of Mangetic Materials*; Buschow, K.H.J., Ed.; Elsevier Science Publishers: Berlin, Germany, 1991; Volume 6, pp. 356–369.
24. Yano, K. Molecular field analysis for melt-spun amorphous $Fe_{100-x}Gd_x$ alloys ($18 \leqq X \leqq 60$). *J. Magn. Magn. Mater.* **2000**, *208*, 207–216. [CrossRef]
25. Yano, K.; Kita, E. Effect of covalent element boron on exchange interaction and magnetic moment in $Fe_{0.4}Gd_{0.6}$ binary alloy. *J. Magn. Magn. Mater.* **2004**, *272*, 1370–1371. [CrossRef]
26. Zhang, H.Y.; Xu, Y.F.; Zhang, Z.Y.; Tan, J.; Zhang, X.; Peng, H.; Xiang, X.J.; Li, H.L.; Xia, A.L.; Li, W.H. Influence of Covalent Element B and Si Addition on Magnetocaloric Properties of Gd-Co-Fe-(B, Si) Amorphous Alloys. *Metals* **2022**, *12*, 386. [CrossRef]
27. Sandeman, K.G.; Takei, S. Magnetocaloric Materials and Applications. In *Handbook of Magnetism and Magnetic Materials*; Coey, M., Parkin, S., Eds.; Springer International Publishing: Cham, Switzerland, 2021; pp. 1489–1526.
28. Ichitsubo, T.; Matsubara, E.; Numakura, H.; Tanaka, K.; Nishiyama, N.; Tarumi, R. Glass-liquid transition in a less-stable metallic glass. *Phys. Rev. B* **2005**, *72*, 052201. [CrossRef]
29. Xue, L.; Li, J.; Yang, W.; Yuan, C.; Shen, B. Effect of Fe substitution on magnetocaloric effects and glass-forming ability in Gd-based metallic glasses. *Intermetallics* **2018**, *93*, 67–71. [CrossRef]
30. Zheng, Z.G.; Qiu, Z.G.; Zeng, D.C. Effect of Co substitution on thermal stability and magnetocaloric effects of $Gd_{70}Al_{20}Fe_{10-x}Co_x$ amorphous alloys. *Mater. Res. Express* **2019**, *6*, 096109. [CrossRef]

31. Pierunek, N.; Śniadecki, Z.; Marcin, J.; Škorvánek, I.; Idzikowski, B. Magnetocaloric effect of amorphous $Gd_{65}Fe_{10}Co_{10}Al_{10}X_5$ (X = Al, Si, B) alloys. *IEEE Trans. Magn.* **2014**, *50*, 2506603. [CrossRef]

32. Franco, V.; Blázquez, J.S.; Ipus, J.J.; Law, J.Y.; Moreno-Ramirez, L.M.; Conde, A. Magnetocaloric effect: From materials research to refrigeration devices. *Prog. Mater. Sci.* **2018**, *93*, 112–232. [CrossRef]

33. Xia, L.; Wu, C.; Chen, S.H.; Chan, K.C. Magneto-caloric effect of a $Gd_{50}Co_{50}$ amorphous alloy near the freezing point of water. *AIP Adv.* **2015**, *5*, 097122. [CrossRef]

34. Zhong, X.; Huang, X.; Shen, X.; Mo, H.; Liu, Z. Thermal stability, magnetic properties and large refrigerant capacity of ternary $Gd_{55}Co_{35}M_{10}$ (M = Mn, Fe and Ni) amorphous alloys. *J. Alloys Compd.* **2016**, *682*, 476–480. [CrossRef]

35. Banerjee, B.K. On a generalised approach to first and second order magnetic transitions. *Phys. Lett.* **1964**, *12*, 16–17. [CrossRef]

36. Griffith, L.D.; Mudryk, Y.; Slaughter, J.; Pecharsky, V.K. Material-based figure of merit for caloric materials. *J. Appl. Phys.* **2018**, *123*, 034902. [CrossRef]

37. Sakka, A.; M'Nassri, R.; Nofal, M.M.; Mahjoub, S.; Cheikhrouhou-Koubaa, W.; Chniba-Boudjada, N.; Oumezzine, M.; Cheikhrouhou, A. Structure, magnetic and field dependence of magnetocaloric properties of $Pr_{0.5}RE_{0.1}Sr_{0.4}MnO_3$ (RE = Eu and Er). *J. Magn. Magn. Mater.* **2020**, *514*, 167158. [CrossRef]

38. Mahjoub, S.; M'nassri, R.; Baazaoui, M.; Hlil, E.K.; Oumezzine, M. Tuning magnetic and magnetocaloric properties around room temperature via chromium substitution in $La_{0.65}Nd_{0.05}Ba_{0.3}MnO_3$ system. *J. Magn. Magn. Mater.* **2019**, *481*, 29–38. [CrossRef]

39. Mitrofanov, V.Y.; Estemirova, S.K.; Kozhina, G.A. Effect of oxygen content on structural, magnetic and magnetocaloric properties of $(La_{0.7}Pr_{0.3})_{0.8}Sr_{0.2}Mn_{0.9}Co_{0.1}O_{3\pm\delta}$. *J. Magn. Magn. Mater.* **2019**, *476*, 199–206. [CrossRef]

40. Shishkin, D.A. Magnetothermal properties of iron-based amorphous alloys type of $Fe_{63.5}M_{10}Si_{13.5}B_9Nb_3Cu_1$ (M = Cr, Mn, Fe, Co, Ni). *Mater. Res. Express* **2019**, *6*, 025201. [CrossRef]

41. Dan'kov, S.Y.; Tishin, A.M.; Pecharsky, V.K.; Gschneidner, K.A., Jr. Magnetic phase transitions and the magnetothermal properties of gadolinium. *Phys. Rev. B* **1998**, *57*, 3478–3490. [CrossRef]

42. Wang, Y.F.; Duc, N.T.M.; Feng, T.F.; Wei, H.J.; Qin, F.X.; Phan, M.H. Competing ferromagnetic and antiferromagnetic interactions drive the magnetocaloric tunability in $Gd_{55}Co_{30}Ni_xAl_{15-x}$ microwires. *J. Alloys Compd.* **2022**, *907*, 164328. [CrossRef]

43. Yano, K.; Akiyama, Y.; Tokumitsu, K.; Kita, E.; Ino, H. Magnetic moment and Curie temperature for amorphous $Fe_{100-x}Gd_x$ alloys ($18 \leqq x \leqq 60$). *J. Magn. Magn. Mater.* **2000**, *214*, 217–224. [CrossRef]

44. Madsen, K.; Nielsen, H.B.; Tingleff, O. *Methods for Non-Linear Least Squares Problems*, 2nd ed.; Informatics and Mathematical Modelling; Technical University of Denmark: Lyngby, Denmark, 2004.

45. Hassini, A.; Lassri, H.; Bouhdada, A.; Ayadi, M.; Krishnan, R.; Mansouri, I.; Chaker, B. Magnetic coupling in amorphous $Fe_{80-x}Gd_xB_{20}$ alloys. *Phys. B Condens. Matter.* **2000**, *275*, 295–300. [CrossRef]

46. Ishio, S.; Obara, N.; Negami, S.; Miyazaki, T.; Kamimori, T.; Tange, H.; Goto, M. Magnetic properties and exchange interactions in $(Gd_xFe_{1-x})_{80}Si_{12}B_8$ amorphous alloys. *J. Magn. Magn. Mater.* **1993**, *119*, 271–278. [CrossRef]

47. Lee, J.M.; Jung, J.K.; Lim, S.H. Mean field analysis of exchange coupling in amorphous $DyFe_2$-B alloy ribbons. *J. Magn. Magn. Mater.* **2001**, *234*, 133–141. [CrossRef]

48. Lu, S.; Zhang, J.; Duan, H. Effects of B substitution for P on structure and magnetic properties of FePB amorphous alloys by first-principle investigation. *Intermetallics* **2022**, *149*, 107674. [CrossRef]

49. Yaocen, W.; Yan, Z.; Makino, A.; Yunye, L.; Kawazoe, Y. Structural and Magnetic Study of $Fe_{76}Si_9B_{10}P_5$ Metallic Glass by First Principle Simulation. *IEEE Trans. Magn.* **2014**, *50*, 1–4. [CrossRef]

50. Tian, H.; Zhang, C.; Zhao, J.; Dong, C.; Wen, B.; Wang, Q. First-principle study of the structural, electronic, and magnetic properties of amorphous Fe–B alloys. *Phys. B Condens. Matter.* **2012**, *407*, 250–257. [CrossRef]

51. De Boer, F.R.; Mattens, W.C.M.; Boom, R.; Miedema, A.R.; Niessen, A.K. *Cohesion in Metals: Transition Metal Alloys*; Elsevier Science Publishers: Amsterdam, The Netherlands, 1988.

52. Li, H.X.; Lu, Z.C.; Wang, S.L.; Wu, Y.; Lu, Z.P. Fe-based bulk metallic glasses: Glass formation, fabrication, properties and applications. *Prog. Mater. Sci.* **2019**, *103*, 235–318. [CrossRef]

53. Campbell, I.A. Indirect exchange for rare earths in metals. *J. Phys. F Metal Phys.* **1972**, *2*, L47–L50. [CrossRef]

54. McHenry, M.E.; Willard, M.A.; Laughlin, D.E. Amorphous and nanocrystalline materials for applications as soft magnets. *Prog. Mater. Sci.* **1999**, *44*, 291–433. [CrossRef]

55. Hasegawa, R.; Taylor, R.C. Magnetization of amorphous Gd-Co-Ni films. *J. Appl. Phys.* **1975**, *46*, 3606–3608. [CrossRef]

56. Schwarz, B.; Mattern, N.; Luo, Q.; Eckert, J. Magnetic properties and magnetocaloric effect of rapidly quenched Gd-Co-Fe-Al alloys. *J. Magn. Magn. Mater.* **2012**, *324*, 1581–1587. [CrossRef]